Magnetic Nanobeads as Potential Contrast Agents for Magnetic Resonance Imaging

Michele H. Pablico-Lansigan,[†] William J. Hickling,[†] Emily A. Japp,[†] Olga C. Rodriguez,[§] Anup Ghosh,[§] Chris Albanese,[§] Maki Nishida,[‡] Edward Van Keuren,[‡] Stanley Fricke,[⊥] Norman Dollahon,[∥] and Sarah L. Stoll[†,*]

[†]Department of Chemistry, Georgetown University, 37th and O Streets NW, Washington, D.C. 20057, United States, [‡]Department of Physics, Georgetown University, Washington, D.C. 20057, United States, [§]Lombardi Comprehensive Cancer Center, Georgetown University Medical Center, Washington, D.C. 20057, United States, [⊥]Children's National Medical Center, George Washington University, Washington, D.C. 20010, United States, and [∥]Department of Biology, Villanova University, Villanova, Pennsylvania 19085, United States

ABSTRACT Metal-oxo clusters have been used as building blocks to form hybrid nanomaterials and evaluated as potential MRI contrast agents. We have synthesized a biocompatible copolymer based on a water stable, nontoxic, mixed-metal-oxo cluster, $Mn_8Fe_4O_{12}(L)_{16}(H_2O)_4$, where L is acetate or vinyl benzoic acid, and styrene. The cluster alone was screened by NMR for relaxivity and was found to be a promising T_2 contrast agent, with $r_1 = 2.3\ mM^{-1}\ s^{-1}$ and $r_2 = 29.5\ mM^{-1}\ s^{-1}$. Initial cell studies on two human prostate cancer cell lines, DU-145 and LNCap, reveal that the cluster has low cytotoxicity and may be potentially used *in vivo*. The metal-oxo cluster $Mn_8Fe_4(VBA)_{16}$ (VBA = vinyl benzoic acid) can be copolymerized with styrene under miniemulsion conditions. Miniemulsion allows for the formation of nanometer-sized paramagnetic beads (~80 nm diameter), which were also evaluated as a contrast agent for MRI. These highly monodispersed, hybrid nanoparticles have enhanced properties, with the option for surface functionalization, making them a promising tool for biomedicine. Interestingly, both relaxivity measurements and MRI studies show that embedding the Mn_8Fe_4 core within a polymer matrix decreases r_2 effects with little effect on r_1, resulting in a positive T_1 contrast enhancement.

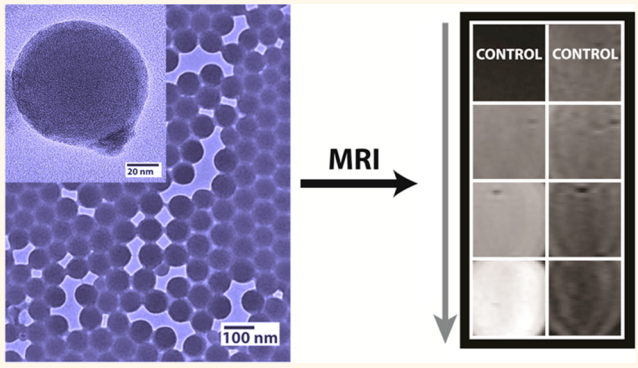

KEYWORDS: miniemulsion nanobeads · manganese oxo clusters · contrast agents

Magnetic resonance imaging (MRI) is a powerful diagnostic tool used in both clinical and research applications to map the tissues and organs in the body.[1] The contrast in MR depends on the proton spin density and the longitudinal (T_1) and transverse (T_2) relaxation times. The T_1-weighted or T_2-weighted images can be significantly enhanced by a contrast agent. The clinically used gadolinium chelates shorten T_1, which increases the concentration-dependent relaxivity r_1, (inverse of T_1), causing a brightening effect in MR.[2] Alternatively, superparamagnetic iron oxide nanoparticles can be used, which shorten T_2 (increase r_2), leading to signal reduction resulting in a darkening effect.[3,4] There is also an additional dephasing effect that comes from the magnetic field inhomogeneity, referred to as T_2^*, often shorter than T_2.[5]

The past decade has seen many efforts to create novel systems for contrast agents, and several design strategies stand out. Consistently, metals have been chosen for high spin states (molecular contrast agents) or large net moment (for nanoparticles), with the assumption that toxicity and targeting can be controlled either through the chelating ligand (molecular) or surface ligands (nanoparticles). The magnetic moment is one of the dominant factors determining relaxivity, and of course the greater the relaxivity, the stronger the signal and lower concentrations of contrast agent required. The mechanism for T_1 contrast

* Address correspondence to sls55@georgetown.edu.

Received for review July 16, 2013 and accepted September 18, 2013.

Published online September 18, 2013
10.1021/nn403647t

agents is primarily direct proton interaction, so the relaxivity is affected by the number of open sites at the metal (according to the Solomon Bloemenbergen Morgan theory).[6,7] However, for a T_2 contrast agent, the bulk susceptibility effect creates a local magnetic field experienced by the water protons,[8] and proximity is less important (r^{-2} *vs* r^{-6}).[2] While there is strong motivation to reduce the total amount of metal, having a high density of contrast at a specific location is highly sought after.

Generally, the paramagnetic chelates act as the more desirable T_1 contrast agent; however, there is strong interest in identifying alternatives to gadolinium for patients with chronic kidney disease (CKD)[9,10] as a result of toxicity (nephrogenic systemic fibrosis)[11−13] and environmental concerns.[14,15] For oncology diagnosis, paramagnetic chelates are limited by circulation time and contrast, so magnetic nanoparticles have been favored for such applications.[16] Magnetic nanoparticles bring several advantages to contrast agents both because of the strong effect on relaxivity, and the ability to tailor the magnetic properties by choice of magnetic core, size, as well as flexibility in the design of surface chemistry. Importantly, the surface provides a means for coupling multifunctional components such as receptor targets (labeled antibodies,[17] or folate receptors),[18] fluorescent probes[19] for optical tracking, or finally therapeutic drugs (*e.g.*, doxorubicin).[20] Iron oxide nanoparticles have found important applications in *in vivo* cell tracking[21] and stem cell labeling in animal models.[22] Techniques to monitor breast and prostate tumor progression using MRI have been developed using superparamagnetic iron oxide contrast agents. For example, it has been demonstrated that iron oxide nanoparticles in polymer microspheres can label, follow cell proliferation, and be used to monitor tumor formation.[23] However, one of the major limitations to this method is the inhomogeneity of the iron oxide content within each nanobead. Because T_2 contrast agents reduce signal, leading to false readings is one reason iron oxide contrast agents have not become widespread for use in cancer imaging, despite some initial successes.[24] While superparamagnetic iron oxide nanoparticles such as Feridex I.V. are FDA approved for detecting liver metastases, the commercial development of new iron oxide based nanoparticles as contrast agents has failed to progress.

Because of the limitations of gadolinium and iron oxide based agents, interest has returned to manganese.[25−29] Manganese has a long history as a contrast agent as first proposed by Lauterbur.[30] The first criteria for a contrast agent, strong paramagnetism, is met by the high spin d^5 Mn(II) but is difficult to coordinate because of lability. The smaller size of Mn(II) compared with Gd(III) limits the extent to which the chelate effect can overcome this.[31] There have been a few commercial contrast agents based on Mn chelates, such as Teslascan,[32] or Mn-DPDP (where DPDP is an aminocarboxylate multidentate ligand).[33] However, many other complexes of Mn(II) such as analogues of EDTA[34] or DTPA as well as macrocyclic ligands have been investigated.[29] High relaxivities have also been observed in the lower spin state Mn(III) complexes of sulfonated porphyrins.[35]

More recently, efforts to prepare nanoscale contrast agents based on manganese have been explored for enhanced relaxivity. Novel systems such as manganese dichloride incorporated into liposomes,[36] the flexible system based on nanoscale metal oxide frameworks (NMOFs),[37] or Mn-substituted polyoxometalates (POMs),[38] have exhibited promising relaxivities but have issues of metal leaching. Nanoparticles most typically result in T_2 contrast agents, with few exceptions such as the series of MnO nanoparticles that have been found to exhibit novel T_1 contrast.[39] Unlike most magnetic nanoparticles, the relaxivity of MnO nanoparticles appears to increase with decreasing particle size, and the antiferromagnetic core significantly reduces susceptibility artifacts. The relaxivity is thought to be proportional to the number of Mn(II) ions on the surface of the MnO nanoparticles; however, an alternative explanation for the T_1 brightening effect is the slow dissolution of Mn(II).[40] One of the limitations of manganese is that overexposure can cause Parkinson-like symptoms termed "Manganism".[41] Therefore, controlling metal leaching is a critical issue in design of magnetic nanostructures.

Clusters, which harbor several distinct MR contrast entities, open a new avenue for exploring contrast agents with the ability to deliver multiple metals to a target site. One of the earliest clusters studied was based on the single molecule magnet $[Fe_8(tacn)_6O_2(OH)_{12}]Br_8$ or Fe_8.[42] The relaxivity is modest (r_1 of 1.2 mM^{-1} s^{-1}),[43] and has the advantage that the molecule acts as a T_1 contrast agent. However, Fe_8 has a limited solubility range, and the disadvantage that the ligand is not easily tailored without altering the core structure. On the other hand, one of the unique aspects of the single molecule magnet, $Mn_{12}O_{12}(O_2CCH_3)_{16}(H_2O)_4$ or Mn_{12}, is that it easily undergoes ligand exchange. The properties due to the core are only modestly affected by ligand exchange, and the importance is that ligand exchange provides a synthetic tool for the intact cluster to be modified or grafted to nanostructured materials.[44] For example, Mn_{12} has been coordinated to the surface of a polymer bead, or encapsulated by an emulsion-assisted assembly for MRI studies.[45,46] Although Mn_{12} gains stability by surface attachment, the cluster alone readily forms a flocculent precipitate in water. While the aqueous relaxivity of Mn_{12} has been studied, aqueous stability requires high concentrations of acetic acid that may affect these measurements.

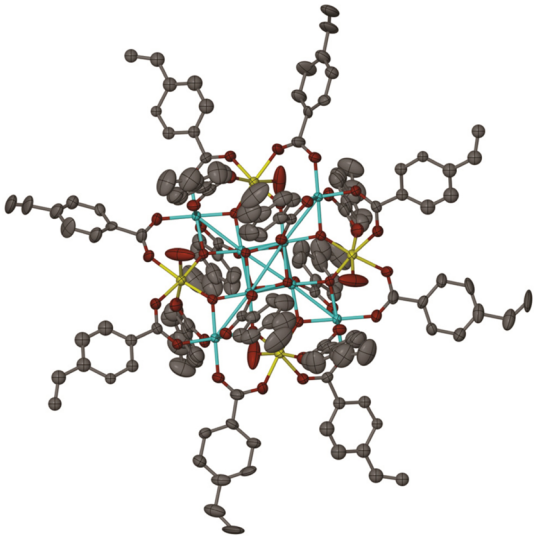

Figure 1. Thermal ellipsoid plot of the refinement model of structure of $Mn_8Fe_4O_{12}(VBA)_{16}$ at 70% probability. Only major occupancies are shown. Cocrystallized solvents and hydrogen atoms were excluded for clarity. Code for atoms: aqua, Mn; yellow, Fe; red, O; and gray, C.

We have discovered recently that incorporation of the biologically benign metal iron into Mn_{12} (the previously reported $Mn_8Fe_4O_{12}(O_2CCH_3)_{16}(H_2O)_4$ or Mn_8Fe_4)[47] increases the spin state (8.58 μ_{eff}/molecule) due to the substitution of Fe^{3+} ($S = 5/2$) for Mn^{3+} ($S = 2$). Importantly, the iron substitution confers aqueous solubility and stability of the cluster. As these clusters undergo similar ligand exchange chemistry as Mn_{12}, we have taken advantage of this to synthesize magnetic nanobeads prepared as copolymers of $Mn_8Fe_4O_{12}$-$(VBA)_{16}$ (VBA = vinyl benzoic acid, see Figure 1), with styrene.[48]

Herein, we focus on the development and characterization of iron-substituted metal-oxo cluster, Mn_8-$Fe_4O_{12}(VBA)_{16}$-co-styrene copolymer nanobeads as potential MRI contrast agent. Using the miniemulsion polymerization technique, nanometer-sized beads were prepared. We were able to incorporate the substituted cluster into the polymeric polystyrene matrix *via* cross-linking the olefin functionality of vinyl benzoic acid ligand with styrene to form metal-oxo copolymer nanobeads. The significance is that cross-linking the cluster effectively prevents metal leaching.[49,50] The $Mn_8Fe_4(VBA)_{16}$ is soluble in styrene, so the resulting nanobeads have homogeneously dispersed metal (unlike Fe_3O_4-styrene nanobeads), which is critical for high resolution imaging. Another advantage of these paramagnetic copolymer nanobeads is that the cluster has a fixed magnetic core, which means the magnetic properties are independent of the size of the bead. This distinguishes these nanobeads from superparamagnetic iron oxide nanoparticles where the magnetic properties are very sensitive to size. Using miniemulsion, the bead diameter can be dialed in to any size from 50 to 500 nm.[51] This is a significant advantage because contrast agents are being developed for specific applications, and researchers need a distinct range of diameters for a particular application without diminishing the magnetic properties.

The cluster and the copolymer beads have been screened as a potential MRI contrast agent by both NMR and phantom MRI studies and found to have promising properties. Initial cell studies on two human prostate cancer cell lines, DU-145 and LNCaP, reveal that the cluster has low cytotoxicity and may be potentially used *in vivo*. Interestingly, relaxivity measurements and MRI studies show that encapsulating the Mn_8Fe_4 core within a polymer matrix decreased r_2 effects with limited effects on r_1, resulting in a positive T_1 contrast enhancement. These hybrid nanobeads have the potential for surface functionalization, making them a promising tool for biomedicine.

RESULTS AND DISCUSSION

The design of the magnetic nanobeads used here was intended to maintain several features of commercially available iron oxide nanobeads that have been used in tumor progression by MRI. Notably, polystyrene was selected as the carrier structure, and the bead diameter targeted was ~100 nm. By replacing the nanoparticles with clusters, specific characteristics such as the homogeneity of the inorganic component would be significantly improved. By starting with a soluble, high spin cluster, ligated by carboxylates with olefin functionality, the goal was to fabricate a highly cross-linked, homogeneous copolymer in the form of a size-controlled nanobead.

We have previously described the synthesis of the $Mn_8Fe_4O_{12}(VBA)_{16}$-co-styrene copolymer nanobeads using miniemulsion polymerization method.[48] Reactions using miniemulsion technique resulted in highly monodispersed nanobeads, as supported by dynamic light scattering (DLS) measurements that show a unimodal distribution, and a hydrodynamic diameter of 84.0 ± 0.9 nm. Additionally, the average diameters based on transmission electron microscopy (TEM) were 70.0 ± 9.4 nm (for 200 particles) with a size distribution of 1.05 (see Figure 2). Further, the TEM also indicates that the metal dispersion is highly homogeneous (inset Figure 2). This is in contrast to polystyrene nanobeads of iron oxide nanoparticles, which exhibit random inclusion of small particles within the matrix.[23] After purification by dialysis, the metal content of the copolymer beads was found to be 1.67% Mn, and 0.97% Fe, as expected for the starting $Mn_8Fe_4O_{12}(VBA)_{16}$:styrene ratio of 1:200. The dialysis experiments also allowed us to measure the metal content in solution over time (using atomic absorption of aliquots from the solution). We did not observe any metal leaching from copolymer nanobeads. In addition, we have monitored the T_1 and T_2 of the magnetic nanobeads over a period

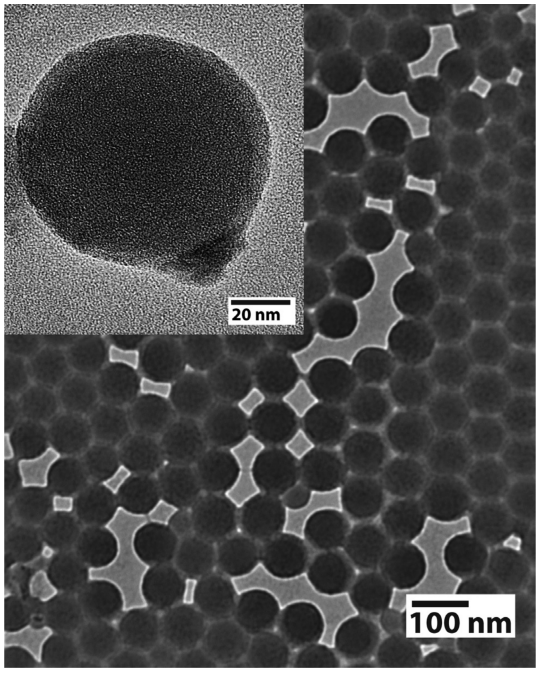

Figure 2. TEM of $Mn_8Fe_4O_{12}(VBA)_{16}$-co-styrene copolymer nanobeads. Inset: HR-TEM.

of 2 weeks and observed no significant changes (Supporting Information, Figure S1).

Evidence from several experiments support the fact that the cluster remains intact upon copolymerization. The first is that the infrared spectroscopy (Supporting Information, Figure S2) of the copolymer exhibits characteristic Mn_8Fe_4 core stretching bands at low frequency between 450 and 600 cm^{-1}, as expected for the core cluster-breathing mode. The infrared also supports the cross-linking of the $Mn_8Fe_4O_{12}(VBA)_{16}$ cluster as evidenced by the loss of the vinyl band for 4-vinylbenzoic acid cluster ligand, upon polymerization. Finally, we have previously confirmed that analogous nanobeads prepared with $Mn_{12}O_{12}(VBA)_{16}$ remain intact cluster after copolymerization. For these nanobeads, the characteristic single molecule magnet properties due to the core cluster are unchanged (peak in χ'' *versus* T).[48] Several bulk polymers formed with Mn_{12} and other olefin functionalities (acrylic acid or methyl-methacrylic acid) have been reported in the literature with the magnetic properties unaltered.[52,53] Thus, we believe that copolymerization does not substantially alter the structure or magnetic properties of the clusters.

Initial screening of the concentration-dependent T_1 and T_2 was performed using proton NMR. While a large r_1 is important for a T_1-weighted contrast agent, the ratio of r_2:r_1 is important for determining whether a contrast agent is a T_1 or T_2 type (the ratio of r_2:r_1 generally between 1 and 3 is a T_1 type, >10 is a T_2 type).[2] The relaxation rates of the Mn_8Fe_4 cluster in water were measured using an internal, D_2O standard with a 300 MHz NMR, at room temperature

TABLE 1. Comparison of Relaxivity Values, r_1 and r_2, of Mn_8Fe_4 in Different Media

	relaxivity		
solvent	r_1 (mM^{-1} s^{-1})	r_2 (mM^{-1} s^{-1})	r_2/r_1
D_2O	2.38	26.65	11.12
H_2O (with internal D_2O std)	1.80	26.79	14.9
0.5 mM deuterated BSA	2.92	29.77	10.2

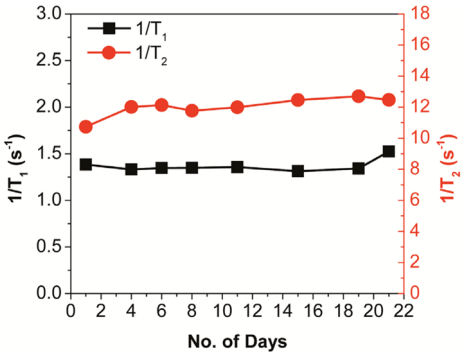

Figure 3. Relaxivity values of Mn_8Fe_4 (0.3 mM metal) in D_2O monitored for several days as a measure of cluster aqueous stability.

(see Supporting Information, Figure S3). The relaxivity values (r_1, r_2) are listed in Table 1. The r_1 relaxivity for Mn_8Fe_4 is only slightly lower than Mn-DPDP, and consistent with the range found for other (high spin d^4/d^5) molecular contrast agents.[54] The r_2 is significantly higher than seen in molecular systems (for example, almost an order of magnitude higher than Mn-DPDP), potentially indicating a bulk susceptibility effect. In addition, we measured the r_1 and r_2 of the cluster over the course of 30 days and found the values were reasonably consistent, indicating aqueous solution stability (see Figure 3). These data are consistent with the MRI (7T Bruker Biospin) phantom images obtained from the cluster dissolved in agar. In T_1 weighted images, there is no measurable effect with increasing concentration of the Mn_8Fe_4 cluster, but as expected from the NMR data, the T_2-weighted images exhibit a strong darkening effect with increasing concentration (see Figure 4A). To investigate the influence of the environment, the relaxivity properties were also measured in D_2O and bovine serum albumin (BSA) (Supporting Information, Figure S3). The D_2O was used for locking,[55] but more importantly to avoid both receiver saturation and radiation damping effects.[43] The relaxivity was also measured in BSA in order to mimic the biological fluid environment. Serum albumin is the richest protein in human blood plasma and plays a critical role in the uptake, transportation, biodistribution and excretion of the contrast agent in the human body.[38] Given the ratio of r_1:r_2 ($\gg$1), and the resulting phantom MRI images, we conclude that the

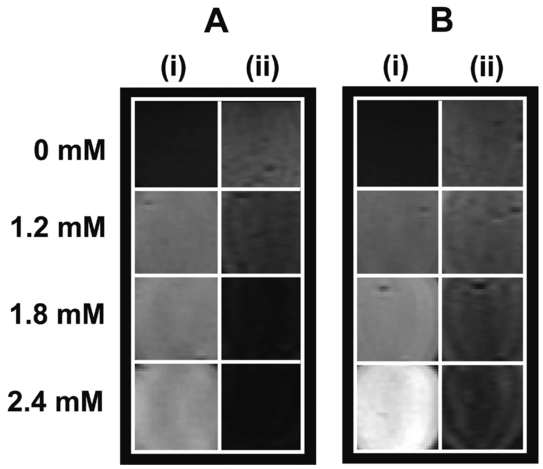

Figure 4. *In vitro* T_1 (i) and T_2 (ii) weighted MRI of (A) Mn_8Fe_4 and (B) $Mn_8Fe_4O_{12}(VBA)_{16}$-co-styrene copolymer nanobeads in 3% agar. The percent intensity change for these graphs are provided in the Supporting Information.

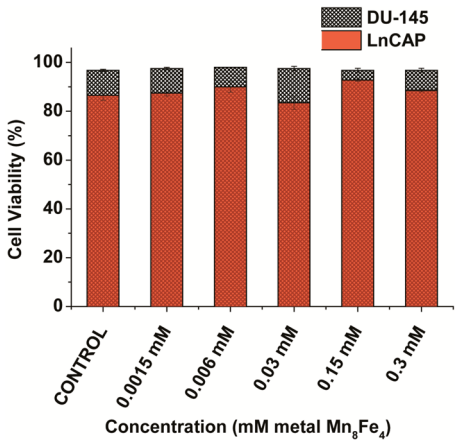

Figure 5. Cell viability of Mn_8Fe_4 at various metal concentrations. Human-derived prostate cancer cell lines were used: (gray) DU-145, (red) LnCap.

Mn_8Fe_4 cluster acts as a T_2 contrast agent, with modest variation due to the solution environment.

In order to be useful as a building block in designing magnetic nanobeads as MRI contrast agents, it is critical to assess the cytotoxicity of the cluster. Thus, cell studies were performed using two human prostate cancer cell lines, DU-145 (androgen-insensitive human prostate cancer cell line) and LNCaP (androgen-responsive human prostate adenocarcinoma cell lines). Cells were incubated with the cluster and trypsinized. The cell viability was determined using a dye exclusion method (Trypan blue). As seen in Figure 5, the viability of the prostate cancer cells in the presence of the cluster over a range of 0.0015−0.3000 mM was indistinguishable from control, untreated cells. These results strongly support that the cluster is inert, at least *in vitro*.[23]

The size of magnetic nanoparticles has a strong influence in biodistribution and function.[56] Grafting the Mn_8Fe_4 clusters into the polystyrene to form copolymer nanobeads caused changes in both r_1 and r_2. As has been seen previously for Gd chelates, where r_1 increases with molecular diameter, we observe a modest increase in r_1 from 2.38 to 3.37 mM^{-1} s^{-1} for the nanobeads (see Supporting Information, Figure S4). The increase in r_1 with increasing diameter is normally attributed to the decrease in rotation correlation time as molecular weight or diameter increase.[2] Nanoparticles typically exhibit an increase in r_2 with increasing size for diameters in the "motional averaging regime".[57] However, compared with the cluster that has an r_2 of 26.65 mM^{-1} s^{-1}, the nanobead exhibits a *decrease* in r_2 to 11.07 mM^{-1} s^{-1} (see Supporting Information, Figure S4). For magnetic nanoparticles, size has an important influence over the magnetic moment because it can affect both core crystallinity and the domain size.[58] Generally, smaller particles have smaller magnetic moments, which correspond to a smaller r_2.[59] This has been observed in Fe_3O_4 (magnetite) nanoparticles where decreasing the size from 12 to 4 nm decreases the net saturation magnetization (102 emu/g to 25 emu/g), and the r_2 also decreases.[60] The magnetization rather than the size is key, as seen in the series MFe_2O_4, where M = Mn, Co, Ni where the size of the nanoparticle is kept constant. In this case, as the net moment decreases (due to the differing magnetic contribution of M), the relaxivity also decreases.[61] Here, the size of the nanobead diameter has no effect on μ_{eff}/molecule, so this seems unlikely to be responsible for the change in r_2.

The polymer surface of the copolymer nanobeads could play an important role in relaxivity, as surface coating of nanoparticles have been shown to influence this property.[62] Surface effects[63] in iron oxide nanoparticles can reduce the saturation magnetization, coercivity and the volume of magnetic material,[64] as a result of either oxidation of the surface,[65] magnetic disorder or spin canting in the inorganic surface layer.[66] It can be difficult to separate effects of the organic coating in Fe_3O_4, because the coordinating anchor can modify the surface. However, studies have shown that the organic outer layer has a separate and important role in relaxivity because the coating can influence the rate of water diffusion.[67] It has recently been demonstrated that coating thickness and hydrophilicity (for the same core) influence relaxivity.[68] Exclusion of water by an inner hydrophobic layer can cause a reduction in r_2 value, while a slowing of water diffusion can increase r_2.[67] Here, we believe the hydrophobic polystyrene appears to diminish the value of r_2 perhaps by excluding water. What is interesting is that the effect on r_2 (which is generally thought to be less distant-dependent) is greater than on r_1, with the surprising consequence that the resulting r_2:r_1 is closer to that of a positive contrast agent. The strength of the magnetic nanobeads as a positive contrast agent was

also confirmed in phantom MRI images in agar. Both concentration-dependent T_1-weighted and T_2-weighted MRI images were determined (see Figure 4B). There is a clear brightening effect in the T_1-weighted images, while the T_2-weighted images do not exhibit much of a change with concentration.

In an effort to create a nanobead with a hydrophilic coating, we prepared dextran-coated $Mn_8Fe_4O_{12}$-$(VBA)_{16}$-co-styrene copolymer nanobeads. Dextran is a popular coating for iron oxide nanobeads because it is biocompatible, hydrophilic, and possessing functional groups that are easily modified.[4,69] The dextran-coated $Mn_8Fe_4O_{12}(VBA)_{16}$-co-styrene copolymer nanobeads were generated by the addition of dextran to the surfactant mixture in a one-step miniemulsion synthesis. The dextran is thought to coat the surface of the nanobead by noncovalent interactions.[70] Although all other aspects of the synthesis were unchanged (cluster, styrene, hydrophobe, initiator surfactant concentration), the size of the resulting dextran-coated nanobeads was significantly larger, ~165 nm by DLS. In preliminary studies, the longitudinal relaxivity of the dextran-coated beads (see Supporting Information, Figure S5) increases from 3.37 for uncoated to 6.72 mM^{-1} s^{-1} for the dextran-coated nanobeads. This increase in relaxivity may be due to size (80 nm for uncoated *vs* 165 for coated nanobeads) or the increase in hydrophilicity of the coat. The r_2 also increases with dextran coating from 11.07 for uncoated to 26.00 mM^{-1} s^{-1} for dextran-coated nanobeads (see Supporting Information, Figure S5). Consistent with the measured r_2:r_1 by NMR (3.87 for dextran-coated nanobeads), both the dextran-coated and uncoated nanobeads appear to work as T_1 contrast agents in the phantom MRI images.

CONCLUSIONS

We have developed a novel platform for manganese as a contrast agent. We have found the cluster Mn_8Fe_4 to be a promising building block for preparing MRI contrast agents and miniemulsion technique to be ideal in creating a polystyrene carrier bead with a controllable diameter. The cluster is nontoxic, water stable, and able to undergo ligand exchange providing a means for cross-linking with a biocompatible polymer (polystyrene). The cross-linking of clusters is significant for preventing metal leaching in this system, which remains as a challenge for manganese nanoparticles. The relaxivity appears to be relatively unaffected by the presence of BSA, and the phantom MRI indicate the cluster alone acts as a T_2 contrast agent. Surprisingly, the cluster in the copolymer nanobead has properties that more closely define it as a T_1 contrast agent. Nanobead size effects and the mechanism of relaxivity will be explored in future work.

METHODS

Materials. Fe(II) acetate, potassium permanganate, 4-vinylbenzoic acid, dichloromethane, heptane, ethanol, hexane, acetone, glacial acetic acid, sodium dodecyl sulfate (SDS), hexadecane, 2,2′-azobis(isobutyronitrile) (AIBN), toluene, HCl and tetrahydrofuran (THF) were all purchased from Aldrich and used as received. Styrene and divinylbenzene (DVB) were also purchased from Aldrich, and their inhibitors were removed by filtering through a column of Al_2O_3. Iron and manganese standards for AAS were obtained from Fluka. Dextran 40 (mol wt 40 000), was obtained from TCI.

$Mn_8Fe_4O_{12}(O_2CCH_3)_{16}(H_2O)_4$ was synthesized in our lab, according to the literature.[17] Briefly, Fe(II) acetate (16.3 mmol) was added to a solution of 60% (v/v) acetic acid/H_2O (40 mL) at room temperature, forming a brown slurry. Freshly ground $KMnO_4$ (6.4 mmol) was added to the reaction mixture with stirring for approximately 2 min, followed by heating to 60 °C, yielding a deep golden-brown solution. The resulting solution was cooled to room temperature, layered with 40 mL of acetone, and stored in the dark. After 36 h, black, rod-like single crystals appeared, which were washed with copious amount of acetone and collected by vacuum filtration.

Synthesis of $Mn_8Fe_4O_{12}(OOCC_6H_4CH{=}CH_2)_{16}$ *(*$Mn_8Fe_4O_{12}$-$(VBA)_{16}$*).* This substituted Mn_{12} cluster was previously synthesized by our group.[8] In a typical synthesis, 4-vinylbenzoic acid (2 mmol) was added to a slurry of $Mn_8Fe_4O_{12}(O_2CCH_3)_{16}(H_2O)_4$ (0.125 mmol) in 50 mL of CH_2Cl_2 and stirred for 4 h. The reaction mixture was then filtered to remove any unreacted starting material. The resulting filtrate was layered with 50 mL of ethanol and 50 mL of hexane. After about 3 days, brown solids emerged, which were subjected to a second round of ligand exchange to ensure complete ligand substitution. This was done by redissolving the brown powder in 50 mL of CH_2Cl_2 and adding 4-vinylbenzoic acid, stirring again for 4 h. The solution was filtered and layered with 50 mL of ethanol and 50 mL of hexane. After another 3 days black microcrystals appeared, which were washed with copious amounts of ethanol and hexane and isolated *via* vacuum filtration. The product was found to be $Mn_8Fe_4O_{12}(OOCC_6H_4CH{=}CH_2)_{16}(H_2O)_4 \cdot 2CH_2{=}CHC_6H_4CCO_2H \cdot CH_2Cl_2$. A small amount of the product was put in a vial, dissolved in toluene, and capped. The solution was left undisturbed for several months. This allowed for very slow evaporation of the solvent, which resulted in production of large, reddish brown single crystals that are of suitable quality for single crystal X-ray analysis. Calc (Found) for $C_{165}H_{138}Mn_8Fe_4O_{52}Cl_2$: C, 53.75; H, 3.77 (C, 53.20; H, 3.81). IR data (KBr, cm^{-1}): 3431 (br), 3072 (w), 3007 (w), 2926 (w), 1936 (w), 1820 (w), 1694 (w), 1670 (w), 1601 (s), 1519 (s), 1405 (vs), 1183 (s), 1142 (w), 1111 (w), 1016 (w), 990 (w), 916 (w), 864 (w), 791 (s), 719 (s), 603 (s), 534 (m), 520 (m).

Miniemulsion Polymerization. Miniemulsion polymerization of the $Mn_8Fe_4O_{12}(VBA)_{16}$ cluster with styrene was previously reported.[8] In a typical synthesis, $Mn_8Fe_4O_{12}(VBA)_{16}$ (0.045 mmol) was dissolved in styrene (8.7 mmol) and DVB (0.087 mmol) in a small vial. In a separate larger vial, SDS (0.7 mmol) was dissolved in deionized water with stirring at ambient temperature. To the $Mn_8Fe_4O_{12}(VBA)_{16}$/styrene/DVB mixture were added hexadecane (0.13 mmol) and AIBN (0.24 mmol). The two solutions were subsequently combined, and the whole reaction mixture was homogenized with an ultrasound sonicator set at an output of 10 W (speed 5) for 120 s. The reaction vessel was then placed in a water bath set at 60 °C for 6 h. It is important to note that only the pure, fully substituted cluster ($Mn_8Fe_4(VBA)_{16}$) dissolves in styrene; if material does not dissolve (indicating an impurity), phase separation is likely to occur during the polymerization. Phase separation can also occur when there is additional vinyl benzoic acid (which can be difficult to identify as the elemental analysis will only be off a small percent). An example of phase separated material can be seen in Supporting Information, Figure S7. Generally, miniemulsion is highly sensitive to the

ratio of reactants and reaction conditions to obtain homogeneous material.

Dextran-Coated $Mn_8Fe_4O_{12}$-co-styrene Copolymer Nanobeads. In a typical synthesis, $Mn_8Fe_4O_{12}(VBA)_{16}$ (0.159 g, 0.045 mmol) was dissolved in styrene (1.0 mL, 8.7 mmol) and DVB (12.4 mL, 0.09 mmol) in a small vial. In a separate larger vial, SDS (0.205 g, 0.700 mmol) and dextran (0.107 g, 0.003 mM) were dissolved in deionized water with stirring at ambient temperature. To the $Mn_8Fe_4O_{12}(VBA)_{16}$/styrene/DVB mixture were added hexadecane (0.13 mmol) and AIBN (0.24 mmol). The two solutions were subsequently combined, and the whole reaction mixture was homogenized with an ultrasound sonicator set at an output of 10 W (speed 5) for 120 s. The reaction vessel was then placed in a water bath set at 60 °C for 6 h.

Nanobead Purification *via* Dialysis. Spectra/Por7 standard grade regenerated cellulose dialysis membrane (Spectrum Laboratories) was used to purify the miniemulsion nanobeads. The tubing used is seamless and semipermeable, with an approximate cutoff (MWCO) of 10 000 Da and a flat width of 12 mm. The tubing was soaked in a large volume of deionized water for 30 min to remove the sodium azide preservative prior to use. This was followed by rinsing thoroughly with running deionized water. The dialysis tubing is cut into the appropriate length using the formula below:

$$\text{total length} = \left(\frac{\text{sample volume}}{\text{volume/length ratio}}\right) + (\text{additional } 20\,\%) + 4 \text{ cm}$$

For this particular tubing, the volume/length ratio is 0.45 mL/cm. Thus, for a sample volume of 1 mL, the tubing was cut to 6.62 cm. One end of the tube was sealed with a weighted magnetic clamp closure. The sample was then loaded, and the other end was clamped with a standard closure. A reservoir was filled with 100 mL (dialysate volume = 100× of sample volume) of deionized water and placed in a magnetic stirring plate. The dialysis sample was immersed into the reservoir and stirred for 24 h. During the duration of the dialysis, the dialysate (deionized water) was changed after the first 3 h and after 20 h. Dialysis was allowed to continue for 4 h after the last dialysate change. To determine that no more free metals were leaching out, a small amount of the dialysate solution was taken and subjected to AAS. The sample was recovered by carefully pouring out the dialyzed sample into a clean vial. This purified nanobead miniemulsion was then subjected to metal content analysis, NMR relaxation studies, and *in vitro* MRI.

Characterization. Fourier-transform infrared spectroscopy (FTIR) measurements were recorded in the range 4000−400 cm^{-1}, from pressed pellets in KBr on a Nicolet FTIR. A Hitachi H-7600 transmission electron microscope (TEM), equipped with an AMT XR 40B camera and operated at 100 kV, and dynamic light scattering (DLS) were both used to determine particle particle size. The DLS apparatus used in this study utilizes light from a HeNe laser that illuminates dilute suspensions of particles. Light scattered at a fixed angle (usually 90°) is coupled though a narrow bandpass optical filter into a single-mode optical fiber, which leads to a high-sensitivity avalanche photodiode photon counting module (EG&G SPCM-15). The count rates from this detector are analyzed by a hardware autocorrelator (ALV-5000, ALV GmbH, Germany). With standard assumptions, it can be shown that the decay rate of the count rate autocorrelation function is inversely proportional to the particle diffusion coefficient, from which information on the particle size is obtained. Initial calculations of the particle sizes were determined from a single exponential fit to the autocorrelation functions.

Metal content of the miniemulsion copolymer nanobeads was analyzed using atomic absorption spectroscopy (AAS). Instead of drying the samples, a 100 μL aliquot of the actual miniemulsion was added to 5 mL of HCl (37%) and 5 mL of toluene. This mixture was stirred for 4 h at room temperature, after which it was transferred to a separatory funnel and allowed to stand overnight. During this process, the brown color of the copolymer nanobeads leached from the polymer, which settled at the meniscus of the HCl layer, and the acid turned deep yellow. The organic layer was discarded, and the inorganic aqueous HCl layer was used for AAS measurements. From the aqueous HCl layer, 2.5 mL was obtained, and this was diluted to 10 mL with deionized water. This sample was then subjected to AAS measurements. Atomic absorption was measured with a BUCK Scientific Model 200A atomic absorption spectrophotometer. Instrument detection limits for AA are calculated to be 0.099 ppm by calculating 3 times the 95% confidence level. By using a calibration curve prepared from iron and manganese standards (Fluka), the metal content of the miniemulsion copolymer nanobeads was calculated.

NMR Relaxation Studies. NMR relaxation data were obtained using a Bruker AM 300 MHz spectrometer interfaced with a TecMag DSpect aquisition system. The proton relaxivities of $Mn_8Fe_4O_{12}$ were measured in D_2O, in H_2O using an internal D_2O standard (pH unadjusted from 4.24), and in 0.5 mM deuterated bovine serum albumin (BSA) solution (pH 5.8). Similarly, the proton relaxivities of the metal-oxo containing polymer nanobeads were measured in D_2O as well (pH 6.8). Fresh solutions of the magnetic cluster and metal-oxo containing polymer nanobeads, with concentrations ranging from 0.6 to 3 mM of metal, were prepared immediately prior to use. For the nanobeads, the Fe and Mn metal content determined from AAS were converted to mM of total metal and summed for the concentration of metal. The measured metal content was close to stoichiometric on the basis of the synthesis; however, relaxivity calculations were determined using analytically determined metal content for each experiment. All the solutions were prepared using serial dilution, and relaxivity measurements were repeated 3 times.

T_1 measurements were recorded using an inversion recovery pulse sequence at room temperature with a least-squares fit to 10 data points. On the other hand, T_2 values were obtained using a conventional spin echo sequence. Relaxivity values, r_1 and r_2, were determined from the slope of a plot of $1/T_1$ or $1/T_2$, respectively, *versus* concentration of $Mn_8Fe_4O_{12}$ in terms of mM metal:

$$\left(\frac{1}{T_i}\right)_{obs} = \left(\frac{1}{T_i}\right) + r_i[\text{M}]$$

where $(1/T_i)$ is the relaxation rate in the presence of the paramagnetic material, $(1/T_i)_0$ is the relaxation rate in the absence of the paramagnetic material, r_i is the relaxivity, and [M] is the concentration in mM metal.

MRI *in Vitro*. Samples with cluster concentrations ranging from 0.6 to 2.4 mM metal (Mn and/or Fe) were prepared in 3% agar and loaded into phantoms. Imaging was performed on a 7T Bruker Biospin (Germany/USA) imaging console equipped with ParaVision v4.0 software. T_1 weighted images were obtained *via* a RARE-T_1 protocol using the following parameters: echo time (TE) 7.5 ms, repetition time (TR) 450 ms, image matrix 256 × 256, slice thickness 1.0 mm, and field of view (FOV) of 8.00 cm. For T_2-weighted imaging, the protocol used was a spin−echo fast imaging technique, TurboRARE-T_2, with the following set of parameters: echo time (TE) 36 ms, repetition time (TR) 4200 ms, image matrix 256 × 256, slide thickness 1.0 mm, and field of view (FOV) of 8.00 cm.

Cytotoxicity Studies. The human prostate cancer derived cell lines, DU-145 and LNCap, were used in this study. The LNCaP cell line is an androgen-responsive human prostate adenocarcinoma cell line, which contains a mutant androgen receptor and is androgen sensitive, whereas the DU-145 cell line is an androgen-insensitive human prostate cancer cell line. Cells were split into six wells containing coverslips and maintained in cell culture media (DMEM for DU-154 and RPMI for LNCap) at 37 °C. Five of the wells containing the cells were incubated with Mn_8Fe_4 (total concentration ranging from 0.0015 mM metal to 0.30 mM metal), while one was left untreated to serve as the control. After 24 h of incubation, cells were washed three times, trypsinized, and resuspended in culture media. This was followed by dilution (1:5) of a small sample of the cell suspension with 0.4% (w/v) trypan blue stain. The cell sample mixed with trypan blue is then loaded into a Countess cell-counting chamber slide. The sample slide is inserted into a Countess automated cell counter, where a built-in camera acquires cell images from the sample on the slide and the image analysis software automatically measures cell count and viability.

The percentage of the viable cells was calculated using the equation below:

$$\% \text{ viability} = \frac{\#\text{ of viable cells counted}}{\text{total cells counted}} \times 100$$

Conflict of Interest: The authors declare no competing financial interest.

Acknowledgment. This research is supported by the NSF Award No. CHE-112387, and X-ray powder diffraction was obtained using an instrument purchased from the MRI program at NSF (CHE-0959546). We acknowledge the support of the Maryland NanoCenter and its NispLab. The NispLab is supported in part by the NSF as a MRSEC Shared Experimental Facility.

Supporting Information Available: The relaxivity values of $Mn_8Fe_4O_{12}$ and $Mn_8Fe_4O_{12}(VBA)_{16}$-co-styrene copolymer nanobeads, monitored over many days, as well as IR spectra of $Mn_8Fe_4O_{12}(VBA)_{16}$-co-styrene copolymer nanobeads. The plot of $1/T_1$, and $1/T_2$ *versus* concentration of Mn_8Fe_4 cluster, Mn_8Fe_4-copolystyrene nanobeads and dextran-coated Mn_8Fe_4-$(VBA)_{16}$-co-styrene nanobeads. Graphs of the percent intensity change as a function of concentration for the phantom MRI. This material is available free of charge *via* the Internet at http://pubs.acs.org.

REFERENCES AND NOTES

1. Strijkers, G.; Mulder, W.; van Tilborg, G.; Nicolay, K. MRI Contrast Agents: Current Status and Future Perspectives. *Anti-Cancer Agents Med. Chem.* **2007**, *7*, 291–305.
2. Caravan, P.; Ellison, J. J.; McMurry, T. J.; Lauffer, R. B. Gadolinium(III) Chelates as MRI Contrast Agents: Structure, Dynamics, and Applications. *Chem. Rev.* **1999**, *99*, 2293–2352.
3. Pankhurst, Q. A.; Connolly, J.; Jones, S. K.; Dobson, J. Applications of Magnetic Nanoparticles in Biomedicine. *J. Phys. D: Appl. Phys.* **2003**, *36*, R167–R181.
4. Laurent, S.; Forge, D.; Port, M.; Roch, A.; Robic, C.; Vander Elst, L.; Muller, R. N. Magnetic Iron Oxide Nanoparticles: Synthesis, Stabilization, Vectorization, Physicochemical Characterizations, and Biological Applications. *Chem. Rev.* **2008**, *108*, 2064–2110.
5. Chavhan, G. B.; Babyn, P. S.; Thomas, B.; Shroff, M. M.; Haacke, E. M. Principles, Techniques, and Applications of T2*-based MR Imaging and Its Special Applications. *Radiographics* **2009**, *29*, 1433–1449.
6. Kowalewski, J.; Nordenskiold, L.; Benetis, N.; Westlund, P. Theory of Nuclear Spin Relaxation in Paramagnetic Systems in Solution. *Prog. NMR Spectrosc.* **1984**, *17*, 141–185.
7. Lowe, M. P. MRI Contrast Agents: The Next Generation. *Aust. J. Chem.* **2002**, *55*, 551.
8. Wolff, S.; Balaban, R. Magnetization Transfer Contrast (MTC) and Tissue Water Proton Relaxation *in Vivo*. *Magn. Reson. Med.* **1989**, *10*, 135–144.
9. Saritas, E. U.; Goodwill, P. W.; Croft, L. R.; Konkle, J. J.; Lu, K.; Zheng, B.; Conolly, S. M. Magnetic Particle Imaging (MPI) for NMR and MRI researchers. *J. Magn. Reson.* **2013**, *229*, 116–126.
10. Manjunath, V.; Perazella, M. A. Imaging Patients with Kidney Disease in the Era of NSF: Can It Be Done Safely? *Clin. Nephrol.* **2011**, *75*, 279–285.
11. Weinreb, J. C.; Abu-Alfa, A. K. Gadolinium-Based Contrast Agents and Nephrogenic Systemic Fibrosis: Why Did It Happen and What Have We Learned? *J. Magn. Reson. Imaging* **2009**, *30*, 1236–1239.
12. Sadowski, E. A.; Bennett, L. K.; Chan, M. R.; Wentland, A. L.; Garrett, A. L.; Garrett, R. W.; Djamali, A. Nephrogenic Systemic Fibrosis: Risk Factors and Incidence Estimation. *Radiology* **2007**, *243*, 148–157.
13. Kuo, P. H.; Kanal, E.; Abu-Alfa, A. K.; Cowper, S. E. Gadolinium-based MR Contrast Agents and Nephrogenic Systemic Fibrosis. *Radiology* **2007**, *242*, 647–649.
14. Serkan, K.; Bau, M. Anthropogenic Gadolinium as a Microcontaminant in Tap Water Used As Drinking Water in Urban Areas and Megacities. *Appl. Geochem.* **2011**, *26*, 1877–1885.
15. Kümmerer, K.; Helmers, E. Hospital Effluents as a Source of Gadolinium in the Aquatic Environment. *Environ. Sci. Technol.* **2000**, *34*, 573–577.
16. Liu, Y.; Solomon, M.; Achilefu, S. Perspectives and Potential Applications of Nanomedicine In Breast And Prostate Cancer. *Med. Res. Rev.* **2010**, *33*, 3–32.
17. Liu, Y.; Chen, Z.; Liu, C.; Yu, D.; Lu, Z.; Zhang, N. Gadolinium-Loaded Polymeric Nanoparticles Modified with Anti-VEGF as Multifunctional MRI Contrast Agents for the Diagnosis of Liver Cancer. *Biomaterials* **2011**, *32*, 5167–5176.
18. Liong, M.; Lu, J.; Kovochich, M.; Xia, T.; Ruehm, S. G.; Nel, A. E.; Tamanoi, F.; Zink, J. I. Multifunctional Inorganic Nanoparticles for Imaging, Targeting, and Drug Delivery. *ACS Nano* **2008**, *2*, 889–896.
19. Holzapfel, V.; Lorenz, M.; Weiss, C. K.; Schrezenmeier, H.; Landfester, K.; Mailander, V. Synthesis and Biomedical Applications of Functionalized Fluorescent and Magnetic Dual Reporter Nanoparticles as Obtained in the Miniemulsion Process. *J. Phys.: Condens. Matter* **2006**, *18*, S2581–S2594.
20. Hong, G.; Yuan, R.; Liang, B.; Shen, J.; Yang, X.; Shuai, X. Folate-Functionalized Polymeric Micelle as Hepatic Carcinoma-Targeted, MRI-Ultrasensitive Delivery System of Antitumor Drug. *Biomed. Microdevices* **2008**, *10*, 693–700.
21. Shapiro, E. M.; Skrtic, S.; Koretsky, A. P. Sizing it up: Cellular MRI Using Micron-Sized Iron Oxide Particles. *Magn. Reson. Med.* **2005**, *53*, 329–338.
22. Shapiro, E. M.; Skrtic, S.; Sharer, K.; Hill, J.; Dunbar, C.; Koretsky, A. P. MRI Detection Of Single Particles For Cellular Imaging. *Proc. Natl. Acad. Sci. U. S. A.* **2004**, *101*, 10901–10906.
23. Rodriguez, O.; Fricke, S.; Chien, C.; Dettin, L.; VanMeter, J.; Shapiro, E. M.; Dai, H.-N.; Casimiro, M.; Ileva, L.; Dagata, J.; *et al.* Contrast-Enhanced *in Vivo* Imaging of Breast and Prostate Cancer Cells By MRI. *Cell Cycle* **2006**, *5*, 113–119.
24. Tassa, C.; Shaw, S. Y.; Weissleder, R. Dextran-Coated Iron Oxide Nanoparticles: A Versatile Platform for Targeted Molecular Imaging, Molecular Diagnostics, and Therapy. *Acc. Chem. Res.* **2011**, *44*, 842–852.
25. Koretsky, A. P.; Silva, A. C. Manganese-Enhanced Magnetic Resonance Imaging (MEMRI). *NMR Biomed.* **2004**, *17*, 527–531.
26. Pan, D.; Schmieder, A. H.; Wickline, S. A.; Lanza, G. M. Manganese-Based MRI Contrast Agents: Past, Present, and Future. *Tetrahedron* **2011**, *67*, 8431–8444.
27. Pan, D.; Caruthers, S. D.; Senpan, A.; Schmieder, A. H.; Wickline, S. A.; Lanza, G. M. Revisiting an Old Friend: Manganese-Based MRI Contrast Agents. *WIREs Nanomed. Nanobiotechnol.* **2010**, *3*, 162–173.
28. Kueny-Stotz, M.; Garofalo, A.; Felder-Flesch, D. Manganese-Enhanced MRI Contrast Agents: From Small Chelates to Nanosized Hybrids. *Eur. J. Inorg. Chem.* **2012**, 1987–2005.
29. Drahoš, B.; Lukeš, I.; Tóth, É. Manganese(II) Complexes as Potential Contrast Agents for MRI. *Eur. J. Inorg. Chem.* **2012**, 1975–1986.
30. Lauterbur, P. Image Formation by Induced local Interactions: Examples Employing Nuclear Magnetic Resonance. *Nature* **2004**, 1–2.
31. Bryant, L. H.; Hodges, M. W.; Bryant, R. G. Test of Electron Delocalization Effects on Water-Proton Spin−Lattice Relaxation by Bromination of [Tetrakis(4-sulfonatophenyl) porphine] Manganese. *Inorg. Chem.* **1999**, *38*, 1002–1005.
32. Krause, W. *Contrast Agents I, Magnetic Resonance Imaging*; Springer-Verlag: New York, 2002; p 165.
33. Federle, M.; Chezmar, J.; Rubin, D. L.; Weinreb, J.; Freeny, P.; Schmiedl, U.; Brown, J.; Borrello, J.; Lee, J. E.-H.; Semelka, R.; *et al.* Efficacy and Safety of Mangafodipir Trisodium (MnDPDP) Injection for Hepatic MRI in Adults: Results of the U.S. Multicenter Phase III Clinical Trials. Efficacy of Early Imaging. *J. Magn. Reson. Imaging* **2000**, *12*, 689–701.
34. Troughton, J. S.; Greenfield, M. T.; Greenwood, J. M.; Dumas, S.; Wiethoff, A. J.; Wang, J.; Spiller, M.; McMurry,

T. J.; Caravan, P. Synthesis and Evaluation of a High Relaxivity Manganese(II)-Based MRI Contrast Agent. *Inorg. Chem.* **2004**, *43*, 6313–6323.
35. Hernandez, G.; Bryant, R. Proton Magnetic Relaxation of Manganese(11)Tetrakis(4-sulfophenyl) Porphrine Ion in Water. *Bioconjugate Chem.* **2001**, 1–4.
36. Niesman, M.; Bacic, G.; Wright, S.; Schwartz, H.; Magin, R. Liposome Encapsulated $MnCl_2$ as a Liver Specific Contrast Agent for Magnetic Resonance Imaging. *Invest. Radiol.* **1990**, *25*, 545.
37. Taylor, K. M. L.; Rieter, W. J.; Lin, W. Manganese-Based Nanoscale Metal−Organic Frameworks for Magnetic Resonance Imaging. *J. Am. Chem. Soc.* **2008**, *130*, 14358–14359.
38. Li, Z.; Li, W.; Li, X.; Pei, F.; Wang, X.; Lei, H. Mn(II)-Monosubstituted Polyoxometalates as Candidates for Contrast Agents In Magnetic Resonance Imaging. *J. Inorg. Biochem.* **2007**, *101*, 1036–1042.
39. Na, H. B.; Lee, J. H.; An, K.; Park, Y. I.; Park, M.; Lee, I. S.; Nam, D.-H.; Kim, S. T.; Kim, S.-H.; Kim, S.-W.; *et al.* Development of a T_1 Contrast Agent for Magnetic Resonance Imaging Using MnO Nanoparticles. *Angew. Chem., Int. Ed. Engl.* **2007**, *46*, 5397–5401.
40. Bennewitz, M. F.; Lobo, T. L.; Nkansah, M. K.; Ulas, G.; Brudvig, G. W.; Shapiro, E. M. Biocompatible and pH-Sensitive PLGA Encapsulated MnO Nanocrystals for Molecular and Cellular MRI. *ACS Nano* **2011**, *5*, 3438–3446.
41. Cersosimo, M. G.; Koller, W. C. The Diagnosis of Manganese-Induced Parkinsonism. *Neurotoxicology* **2006**, *27*, 340–346.
42. Cage, B.; Russek, S. E.; Shoemaker, R.; Barker, A. J.; Stoldt, C.; Ramachandaran, V.; Dalal, N. S. The Utility of the Single-Molecule Magnet Fe8 as a Magnetic Resonance Imaging Contrast Agent over a Broad Range of Concentration. *Polyhedron* **2007**, *26*, 2413–2419.
43. Isaacman, S.; Kumar, R.; Barco, E. D.; Kent, A. D.; Canary, J. W.; Jerschow, A. Critical Examination of Fe8 as a Contrast Agent for Magnetic Resonance Imaging. *Polyhedron* **2005**, *24*, 2691–2694.
44. Steckel, J. S.; Persky, N. S.; Martinez, C. R.; Barnes, C. L.; Fry, E. A.; Kulkarni, J.; Burgess, J. D.; Pacheco, R. B.; Stoll, S. L. Monolayer and Multilayer Films of $[Mn_{12}O_{12}(O_2CMe)_{16}]$. *Nano Lett.* **2004**, *4*, 399–402.
45. Mertzman, J. E.; Kar, S.; Lofland, S.; Fleming, T.; Van Keuren, E.; Tong, Y. Y.; Stoll, S. L. Surface Attached Manganese-Oxo Clusters as Potential Contrast Agents. *Chem. Commun.* **2009**, 788–790.
46. Wang, Y.; Li, W.; Zhou, S.; Kong, D.; Yang, H.; Wu, L. Mn_{12} Single-Molecule Magnet Aggregates as Magnetic Resonance Imaging Contrast Agents. *Chem. Commun.* **2011**, *47*, 3541.
47. Schake, A.; Tsai, H.-L.; Webb, R.; Folting, K.; Christou, G.; Hendrickson, D. N. High-Spin Molecules: Iron(III) Incorporation into $[Mn_{12}O_{12}(O_2CMe)_{16}(H_2O)_4]$ To Yield $[Mn_8Fe_4O_{12}(O_2CMe)_{16}(H_2O)_4]$ and its Influence on the S = 10 Ground State of the Former. *Inorg. Chem.* **1994**, *33*, 6020–6028.
48. Pablico, M. H.; Mertzman, J. E.; Japp, E. A.; Boncher, W. L.; Nishida, M.; Van Keuren, E.; Lofland, S. E.; Dollahon, N.; Rubinson, J. F.; Holman, K. T.; *et al.* Miniemulsion Synthesis of Metal−Oxo Cluster Containing Copolymer Nanobeads. *Langmuir* **2011**, *27*, 12575–12584.
49. Derfus, A. M.; Chan, W. C. W.; Bhatia, S. N. Probing the Cytotoxicity of Semiconductor Quantum Dots. *Nano Lett.* **2004**, *4*, 11–18.
50. Li, H.; Li, P.; Yang, Y.; Qi, W.; Sun, H.; Wu, L. Incorporation of Polyoxometalates Into Polystyrene Latex by Supramolecular Encapsulation and Miniemulsion Polymerization. *Macromol. Rapid Commun.* **2008**, *29*, 431–436.
51. Landfester, K.; Musyanovych, A.; Mailander, V. From Polymeric Particles to Multifunctional Nanocapsules for Biomedical Applications Using the Miniemulsion Process. *J. Polym. Sci., Part A: Polym. Chem.* **2010**, *48*, 493–515.
52. Palacio, F.; Oliete, P.; Schubert, U.; Mijatovic, I.; Hüsing, N.; Peterlik, H. Magnetic Behaviour of a Hybrid Polymer Obtained from Ethyl Acrylate and the Magnetic Cluster $Mn_{12}O_{12}(acrylate)_{16}$. *J. Mater. Chem.* **2004**, *14*, 1873.
53. Willemin, S.; Donnadieu, B.; Lecren, L.; Henner, B.; Clerac, R.; Guerin, C.; Meyer, A.; Pokrovskii, A. V.; Larionova, J. Synthesis and Characterization of Magnetic Organic-Inorganic Nanocomposites Based on the $[Mn_{12}O_{12}\{CH_2C(CH_3)COO\}_{16}(H_2O)_4]$ Building Block. *New J. Chem.* **2004**, *28*, 919.
54. Elizondo, G.; Fretz, C. J.; Stark, D. D.; Rocklage, S. M.; Quay, S. C.; Worah, D.; Tsang, Y. M.; Chen, M. C.; Ferrucci, J. T. Preclinical Evaluation of MnDPDP: New Paramagnetic Hepatobiliary Contrast Agent for MR Imaging. *Radiology* **1991**, *178*, 73–78.
55. Rodríguez, E.; Roig, A.; Molins, E.; Arús, C.; Quintero, M. R.; Cabañas, M. E.; Cerdán, S.; Lopez-Larrubia, P.; Sanfeliu, C. *In Vitro* Characterization of an Fe_8 Cluster as Potential MRI Contrast Agent. *NMR Biomed.* **2005**, *18*, 300–307.
56. Gupta, A. K.; Gupta, M. Synthesis and Surface Engineering of Iron Oxide Nanoparticles for Biomedical Applications. *Biomaterials* **2005**, *26*, 3995–4021.
57. Tromsdorf, U. I.; Bigall, N. C.; Kaul, M. G.; Bruns, O. T.; Nikolic, M. S.; Mollwitz, B.; Sperling, R. A.; Reimer, R.; Hohenberg, H.; Parak, W. J.; *et al.* Size and Surface Effects on the MRI Relaxivity of Manganese Ferrite Nanoparticle Contrast Agents. *Nano Lett.* **2007**, *7*, 2422–2427.
58. Jun, Y.-W.; Seo, J.-W.; Cheon, J. Nanoscaling Laws of Magnetic Nanoparticles and Their Applicabilities in Biomedical Sciences. *Acc. Chem. Res.* **2008**, *41*, 179–189.
59. Jun, Y.-W.; Lee, J. E.-H.; Cheon, J. Chemical Design of Nanoparticle Probes for High-Performance Magnetic Resonance Imaging. *Angew. Chem., Int. Ed.* **2008**, *47*, 5122–5135.
60. Jun, Y.-W.; Huh, Y.-M.; Choi, J.-S.; Lee, J. E.-H.; Song, H.-T.; Kim; Yoon, S.; Kim, K.-S.; Shin, J.-S.; Suh, J.-S.; Cheon, J. Nanoscale Size Effect of Magnetic Nanocrystals and Their Utilization for Cancer Diagnosis *via* Magnetic Resonance Imaging. *J. Am. Chem. Soc.* **2005**, *127*, 5732–5733.
61. Lee, J. E.-H.; Huh, Y.-M.; Jun, Y.-W.; Seo, J.-W.; Jang, J.-T.; Song, H.-T.; Kim, S.; Cho, E.-J.; *et al.* Artificially Engineered Magnetic Nanoparticles for Ultra-Sensitive Molecular Imaging. *Nat. Med.* **2006**, *13*, 95–99.
62. Duan, H.; Kuang, M.; Wang, X.; Wang, Y. A.; Mao, H.; Nie, S. Reexamining the Effects of Particle Size and Surface Chemistry on the Magnetic Properties of Iron Oxide Nanocrystals: New Insights into Spin Disorder and Proton Relaxivity. *J. Phys. Chem. C* **2008**, *112*, 8127–8131.
63. Vestal, C. R.; Zhang, Z. J. Effects of Surface Coordination Chemistry on the Magnetic Properties of $MnFe_2O_4$ Spinel Ferrite Nanoparticles. *J. Am. Chem. Soc.* **2003**, *125*, 9828–9833.
64. Di Marco, M.; Port, M.; Couvreur, P.; Dubernet, C.; Ballirano, P.; Sadun, C. Structural Characterization of Ultrasmall Superparamagnetic Iron Oxide (USPIO) Particles in Aqueous Suspension by Energy Dispersive X-ray Diffraction (EDXD). *J. Am. Chem. Soc.* **2006**, *128*, 10054–10059.
65. Kucheryavy, P.; He, J.; John, V. T.; Maharjan, P.; Spinu, L.; Goloverda, G. Z.; Kolesnichenko, V. L. Superparamagnetic Iron Oxide Nanoparticles with Variable Size and an Iron Oxidation State as Prospective Imaging Agents. *Langmuir* **2013**, *29*, 710–716.
66. Daou, T. J.; Grenèche, J. M.; Pourroy, G.; Buathong, S.; Derory, A.; Ulhaq-Bouillet, C.; Donnio, B.; Guillon, D.; Begin-Colin, S. Coupling Agent Effect on Magnetic Properties of Functionalized Magnetite-Based Nanoparticles. *Chem. Mater.* **2008**, *20*, 5869–5875.
67. Hu, F.; Joshi, H. M.; Dravid, V. P.; Meade, T. J.; High-Performance Nanostructured, M. R. Contrast Probes. *Nanoscale* **2010**, *2*, 1884.
68. LaConte, L. E. W.; Nitin, N.; Zurkiya, O.; Caruntu, D.; O'Connor, C. J.; Hu, X.; Bao, G. Coating Thickness of Magnetic Iron Oxide Nanoparticles Affects R_2 Relaxivity. *J. Magn. Reson. Imaging* **2007**, *26*, 1634–1641.
69. Marie, E.; Rotureau, E.; Dellacherie, E.; Durand, A. From Polymeric Surfactants to Colloidal Systems. *Colloids Surf., A* **2007**, *308*, 25–32.
70. Ladaviere, C.; Averlant-Petit, M. C.; Fabre, O.; Durand, A.; Dellacherie, E.; Marie, E. Preparation of Polysaccharide-Coated Nanoparticles by Emulsion Polymerization of Styrene. *Colloid Polym. Sci.* **2007**, *285*, 621–630.